AIAA 2005-0410

Multimodel Methods for Optimal Control of Aeroacoustics

Guoquan Chen
Rice University
Houston, TX 77005-1892

S. Scott Collis
Sandia National Laboratories[1]
Albuquerque, NM 87185-0370

2005 AIAA Aerospace Sciences Meeting
January 10–13, 2005
Reno, NV

Multimodel Methods for Optimal Control of Aeroacoustics

Guoquan Chen[†]
Rice University
Houston, TX 77005-1892

S. Scott Collis[‡]
Sandia National Laboratories[§]
Albuquerque, NM 87185-0370

A new multidomain/multiphysics computational framework for optimal control of aeroacoustic noise has been developed based on a near-field compressible Navier–Stokes solver coupled with a far-field linearized Euler solver both based on a discontinuous Galerkin formulation. In this approach, the coupling of near- and far-field domains is achieved by weakly enforcing continuity of normal fluxes across a coupling surface that encloses all nonlinearities and noise sources. For optimal control, gradient information is obtained by the solution of an appropriate adjoint problem that involves the propagation of adjoint information from the far-field to the near-field. This computational framework has been successfully applied to study optimal boundary-control of blade-vortex interaction, which is a significant noise source for helicopters on approach to landing. In the model-problem presented here, the noise propogated toward the ground is reduced by 12dB.

Introduction

The coupling of accurate computational fluid dynamics analysis with optimal control theory has the potential to advance active flow-control for complex flows including flows involving aeroacoustic noise generation. In this paper, we report on progress in extending our previous work [1, 2] on aeroacoustic control by using a multi-model approach for optimal control of aeroacoustics. Our motivation is to develop efficient numerical methods to investigate the feasibility of using wall-normal suction/blowing actuation for controlling the Blade-Vortex Interaction (BVI) phenomenon. Rotorcraft BVI typically occurs in low speed, descending flight-conditions (such as on approach to landing) and produces high amplitude, impulsive noise that often dominates other noise sources. Reduction of BVI noise can alleviate restrictions on civil rotorcraft use near city centers and thereby enhance community acceptance.

We have developed an optimal control framework for aeroacoustic applications that will help to identify novel strategies for controlling BVI noise in a systematic manner. The main purpose of aeroacoustic computations is to determine the sound intensity and directivity far away from the noise source. However, the computational cost of using a high-fidelity flow-physics model across such a large domain is usually prohibitive and most researchers resort to some form of multi-physics, domain-decomposition method [3]. For example, in Figure 1 the near-field is obtained by numerical solution of the Navier–Stokes equations while far away from the noise source, where the effects of nonlinearities are negligible, the linearized Euler equations or isentropic wave equation can be used to model the propagating acoustic waves. The interface between the near-field and far-field regions can be accomplished by using a Kirchhoff-type method [4, 5], Lighthill theory and its derivatives [6, 7], or by a direct solution of the linearized Euler equations [8–11]. Applying gradient based optimization in such multi-domain settings is an active research area and derivation of the optimality conditions for multi-domain systems obviously requires an in-depth knowledge of the optimal control formulations for each subsystem. In this paper, our focus is on the formulation and implementation of multi-model/multi-domain methods for optimal control of aeroacoustics with specific application to BVI noise control.

Problem Formulation

Our previous research has included adjoint-based, optimal control of the unsteady compressible Navier–Stokes and Euler equations [1, 12–15] as well as optimal control of unsteady flows based on the Discontinuous Galerkin (DG) Method [2]. Here, we present a multi-domain, multi-model formulation for both state simulation and adjoint-based optimal control using a DG formulation. In this approach, the coupling of multi-domains (near-field and far-field) and multi-models is achieved by weakly enforcing continuity of normal fluxes across a coupling surface using a discontinuous Galerkin approach. The goal of multi-domain/multi-model simulation is to reduce the overall computational cost to simulate the flow by using locally less expensive

[†]Ph.D. Candidate, Department of Mechanical Engineering and Materials Science, gqchen@rice.edu, student member AIAA

[‡]Senior Member of Technical Staff, Optimization and Uncertainty Quantification, sscoll@sandia.gov, Senior Member AIAA.

[§]Sandia is a multiprogram laboratory operated by Sandia Corporation, a Lockheed Martin Company, for the United States Department of Energy's National Nuclear Security Administration under contract DE-AC04-94AL85000.

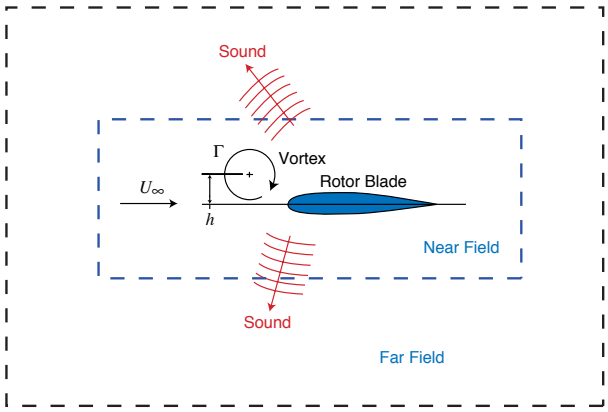

Fig. 1 Blade Vortex Interaction (BVI)

and more computationally efficient physical models without sacrificing the global fidelity of the simulation. Our objective is to develop multi-model simulations using discontinuous Galerkin discretizations for the state and adjoint equations and to use this method within gradient-based optimization algorithms to obtain optimal temporal and spatial distributions of boundary actuation to minimize far-field sound.

The control objective for the problems discussed in this paper targets acoustic waves that are typically several orders of magnitude smaller than the mean flow. This makes linearized methods, such as the linearized Euler equations or the wave equation, appropriate methods for acoustic propagation in the far-field. Because we specifically focus on blowing and suction on the surface of the rotor blade, which may introduce vorticity at the blade surface, we use the full Navier–Stokes equations in the near-field to capture this viscous phenomenon. The use of Navier–Stokes in the near-field limits our current computations to relatively low Reynolds numbers for idealized two-dimensional BVI model problems and our future work will be to extend these methods to increasingly more realistic BVI scenarios.

In general, our multi-model framework is based on a non-overlapping decomposition of the spatial domain and model with the introduction of transmission conditions between the subdomains and submodels that couple the state and adjoint solutions in the optimality system. Both the state and adjoint coupling of the multi-models are achieved by weakly enforcing continuity of normal fluxes across a coupling surface using a DG formulation. Details of the state and adjoint coupling for this multi-domain, multi-model system are discussed in next section. The remainder of this section focuses on the formulation for the state, optimal control problem, and the resulting adjoint equations. In order to simplify the presentation, we limit the discussion to a system that has only two subdomains (i.e., near-field and far-field) where Navier–Stokes is solved in the near-field and the linearized Euler equations are solved in the far-field. However, both our formulation and implementation allow for an arbitrary number of subdomains with a variety of physicals models including Navier–Stokes, Euler, Linearized Navier–Stokes, linearized Euler, and a wave equation. The interested reader should consult [16].

State Equations

The computation domain Ω is divided into two subdomains Ω_{near} in the near-field and Ω_{far} in the far-field. The coupling boundary between these two subdomains is referred to as Γ_c.

In the near-field, the flow is modeled using the compressible Navier–Stokes equations which, in conservative form, are given by

$$\mathbf{U}_{,t}(\mathbf{Y}) + \left(\mathbf{F}_{i,i}(\mathbf{Y}) - \mathbf{F}^v_{i,i}(\mathbf{Y}, \nabla\mathbf{Y})\right) = \mathbf{0} \qquad (1a)$$

in $(t_0, t_f) \times \Omega_{\text{near}}$ with boundary conditions

$$\mathbf{B}_{\text{near}}(\mathbf{Y}, g) = \mathbf{0} \quad \text{on } (t_0, t_f) \times \partial\Omega_{\text{near}}\,, \qquad (1b)$$

where $\mathbf{B}_{\text{near}}$ includes the coupling between near- and far-field subdomains and the transpiration boundary condition on the rotor blade where g is the control variable which is the wall-normal velocity on the rotor-blade in this paper. The initial conditions in the near-field are

$$\mathbf{Y}(t_0, \mathbf{x}) = \mathbf{Y}_0(\mathbf{x}) \quad \text{in } \Omega_{\text{near}} \qquad (1c)$$

where $\mathbf{Y}_0$ is typically a steady-state solution of the Navier–Stokes equations over the rotor blade with a superimposed vortex upstream of the blade as shown schematically in Fig. 1. In equations (1), $\mathbf{n}$ is the unit outward normal vector, $\mathbf{Y} = (\rho, u_1, u_2, T)^{\mathcal{T}}$ is the vector of primitive flow variables, and the conservation variables, expressed as functions of the primitive variables, are given by $\mathbf{U}(\mathbf{Y}) = (\rho, \rho u_1, \rho u_2, \rho E)^{\mathcal{T}}$.

The far-field flow in Ω_{far} is modeled using the linearized Euler equations. We assume that $\mathbf{Y} = \overline{\mathbf{Y}} + \mathbf{y}$ where $\overline{\mathbf{Y}}$ are mean-flow primitive variables and $\mathbf{y}$ are fluctuations in the primitive variables. With this notation, the linearized Euler equations are

$$\overline{\mathbf{M}}\mathbf{y}_{,t} + \left(\overline{\mathbf{A}}_i\overline{\mathbf{M}}\mathbf{y}\right)_{,i} = \mathbf{0} \quad \text{in } (t_0, t_f) \times \Omega_{\text{far}} \qquad (2)$$

where

$$\overline{\mathbf{M}}(\overline{\mathbf{Y}}) = \left.\frac{\partial \mathbf{U}}{\partial \mathbf{Y}}\right|_{\overline{\mathbf{Y}}}$$
$$\overline{\mathbf{A}}_i(\overline{\mathbf{Y}}) = \left.\frac{\partial \mathbf{F}_i}{\partial \mathbf{U}}\right|_{\mathbf{U}(\overline{\mathbf{Y}})}$$

In order to discretize this equation using discontinuous Galerkin, we introduce the quasi-conservative variables $\mathbf{Q}(\mathbf{y}; \overline{\mathbf{Y}}) = \overline{\mathbf{M}}(\overline{\mathbf{Y}})\mathbf{y}$ and recast the linearized Euler equations in the form

$$\mathbf{Q}_{,t}(\mathbf{y}) + \mathbf{F}'_{i,i}(\mathbf{y}) = \mathbf{0} \quad \text{in } (t_0, t_f) \times \Omega_{\text{far}} \qquad (3a)$$

where the flux is given by $\mathbf{F}'_i(\mathbf{y}) = \overline{\mathbf{A}}_i\mathbf{Q}(\mathbf{y})$. Equation (3a) is solved subject to appropriate boundary conditions of the form

$$\mathbf{B}_{\text{far}}(\mathbf{y}) = \mathbf{0} \quad \text{on } (t_0, t_f) \times \partial\Omega_{\text{far}}\,. \qquad (3b)$$

For the problems presented here, the far-field equations are not explicitly dependent on the control variables g which live on the rotor-blade surface. However, $\mathbf{B}'$ does represent the coupling between the near- and far-field subdomains as well as nonreflecting boundary conditions on the outer far-field boundary. Initial conditions for the far-field problem are of the form

$$\mathbf{y}(t_0, \mathbf{x}) = \mathbf{y}_0(\mathbf{x}) \quad \text{in } \Omega_{\text{far}} \tag{3c}$$

where $\mathbf{y}_0$ is typically zero and $\overline{\mathbf{Y}}$ is typically a uniform flow. In the following, we suppress the explicit dependence of far-field quantities on $\overline{\mathbf{Y}}$ unless necessary for clarity.

Given the similarity of (1) and (3), we are able to solve these equations in a unified discontinuous Galerkin framework that is particularly convenient for multi-model simulation and optimization.

Optimal Control Problem

In this paper, we seek to minimize the following objective function

$$\begin{aligned} J(\mathbf{y}, g) \quad = \quad & \frac{\alpha}{2} \int_{t_0}^{t_f} \int_{\Omega_{\text{obs}}} (p')^2 \, d\mathbf{x} \, dt + \\ & \frac{1}{2} \int_{t_0}^{t_f} \int_{\Gamma_g} g^2 \, d\Gamma \, dt \end{aligned} \tag{4}$$

where $p'(\mathbf{x})$ are pressure fluctuations in the far-field and the penalty factor $\alpha = 10^3$. The objective is to minimize the acoustic pressure intensity in $\Omega_{\text{obs}} \subset \Omega_{\text{far}}$ (e.g., see Figure 5) within the time horizon (t_0, t_f). Recall that the control g is exerted on the surface of the rotor blade, Γ_g, and is chosen to be the time and position dependent wall-normal velocity.

Adjoint Equations

We use a gradient-based optimization procedure to solve the optimal control problem represented by minimizing (4) subject to the state equations (1) in the near-field and (3) in the far-field. The gradient is computed using a continuous adjoint method (i.e. the optimize-then-discretize approach). Because of space limitations, we only present a summary of the formulation here and the interested reader should consult [16] for more details.

We begin by introducing the adjoint variables $\boldsymbol{\lambda}$ for the near-field Navier–Stokes equations and $\boldsymbol{\xi}$ for the linearized Euler equations in the far-field. We then define an augmented Lagrangian as

$$\begin{aligned} & L(\mathbf{U}(\mathbf{Y}), \mathbf{Q}(\mathbf{y}), g, \boldsymbol{\lambda}, \boldsymbol{\xi}) = J(\mathbf{y}, g) + \\ & \int_{t_0}^{t_f} \int_{\Omega_{\text{near}}} \boldsymbol{\lambda} \cdot \left(\mathbf{U}_{,t} + \mathbf{F}_{i,i} - \mathbf{F}^v_{i,i} \right) \, d\mathbf{x} \, dt + \\ & \int_{t_0}^{t_f} \int_{\Omega_{\text{far}}} \boldsymbol{\xi} \cdot \left(\mathbf{Q}_{,t} + \mathbf{F}'_{i,i} \right) \, d\mathbf{x} \, dt \end{aligned} \tag{5}$$

and adjoint equations are obtained by taking appropriate variations of the Lagrangian. For example, variation with respect to $\mathbf{Y}$ lead to the adjoint Navier–Stokes equation in the near-field

$$\begin{aligned} & -\boldsymbol{\lambda}_{,t} - (\mathbf{A}_i^T \boldsymbol{\lambda})_{,i} + (\widehat{\mathbf{D}}_i^T \boldsymbol{\lambda})_{,i} - (\widehat{\mathbf{K}}_{ij}^T \boldsymbol{\lambda}_{,j})_{,i} \\ & = \mathbf{A}_{i,i}^T \boldsymbol{\lambda} + \widehat{\mathbf{D}}_{i,i}^T \boldsymbol{\lambda} \qquad \text{in } (t_0, t_f) \times \Omega_{\text{near}} \end{aligned} \tag{6}$$

while variation of (5) with $\mathbf{y}$ yields the adjoint linearized Euler equation in the far-field

$$-\boldsymbol{\xi}_{,t} - \overline{\mathbf{A}}_i^T \boldsymbol{\xi}_{,i} = \mathbf{S} \qquad \text{in } (t_0, t_f) \times \Omega_{\text{far}} \tag{7}$$

where $\mathbf{S}$ depends on variation of the objective functional with $\mathbf{y}$. The interested reader can consult [16] for the definitions of $\mathbf{A}_i$, $\widehat{\mathbf{D}}_i$, $\widehat{\mathbf{K}}_{ij}$, and $\mathbf{S}$.

Adjoint equations (6) and (7) are solved subject to appropriate boundary and final-time conditions and the reader should consult [16] and [13, 14] for details regarding the adjoint boundary conditions on the control surface and the resulting gradient equations. Our focus here is primarily on the multi-domain, multi-model coupling of the State and Adjoint systems. In our formulation, this coupling is achieved naturally by enforcement of weak boundary conditions within our discontinuous Galerkin spatial discretization as discussed in the next section.

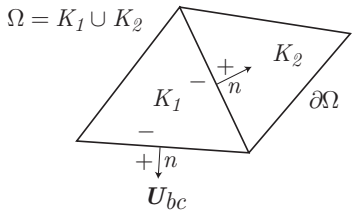

Fig. 2 Schematic of DGM discretization, the solution and weighting functions are discontinuous across element interfaces

Numerical Implementation

Both the State and Adjoint equations are discretized in time with a fourth-order accurate explicit Runge-Kutta method which is symmetric and therefore well-suited for optimal control problems [17]. A high-order accurate, discontinuous Galerkin method is used for spatial discretization. The discontinuous Galerkin method can be thought of as a hybrid of finite-volume and finite-element methods that has a number of potential advantages including: high-order accuracy on unstructured meshes, local hp-refinement, weak imposition of boundary conditions, local conservation, and orthogonal hierarchical bases that support multi-scale and multi-physics modeling. For a recent update on the status of discontinuous Galerkin, the interested reader can consult [18]. For our current purpose, the local conservation property and weak-boundary condition enforcement capabilities of DG are leveraged to simplify the implementation of the multi-model, multi-domain approach.

Weak Formulations

The DG method for the near-field is obtained by starting from the strong form of the compressible Navier–Stokes

equations (1a). Consider a single element, K_e, multiply by a weighting function $\boldsymbol{W}$ that is continuous in K_e, integrate the flux terms by parts, replace the actual flux terms by appropriate numerical fluxes, and sum over all elements $K \in \Omega_{\text{near}}$. Doing so results in the discontinuous Galerkin weak form

$$\sum_{e=1}^{N} \left\{ \int_{K_e} (\boldsymbol{W} \cdot \mathbf{U}_{,t} + \boldsymbol{W}_{,i} \cdot (\mathbf{F}_i^v - \mathbf{F}_i) - \boldsymbol{W} \cdot \mathbf{S}) \, d\mathbf{x} + \int_{\partial K_e} \boldsymbol{W} \cdot \big(\widehat{\mathbf{F}}_n(\mathbf{U}^-, \mathbf{U}^+) - \widehat{\mathbf{F}}_n^v(\mathbf{U}^-, \nabla\mathbf{U}^-, \mathbf{U}^+, \nabla\mathbf{U}^+)\big) \, d\mathbf{s} \right\} = 0 \quad (8)$$

where the $\mathbf{U}^+$ and $\mathbf{U}^-$ states are defined in Figure 2. For an element edge on the subdomain boundary $\partial\Omega_{\text{near}}$, $\mathbf{U}^+ = \mathbf{U}_{bc}$ for an edge coincident with a prescribed boundary condition or, in the case of the coupling boundary between Ω_{near} and Ω_{far}, $\mathbf{U}^+ = \mathbf{U}(\overline{\mathbf{Y}} + \mathbf{y})$ on Γ_c where $\overline{\mathbf{Y}}$ is the mean field and $\mathbf{y}$ is the far-field (perturbation) solution at that edge. Likewise, for inter-element boundaries, $\mathbf{U}^+$ comes from the neighboring element. Thus, all interface and boundary conditions are set through the numerical fluxes. A simple Lax–Friedrichs flux is chosen for the inviscid flux $\widehat{\mathbf{F}}_n$ [19] and we use the method of Bassi & Rebay [20] for the numerical viscous flux $\widehat{\mathbf{F}}_n^v$.

The far-field linearized Euler equations (3a) are also discretized in space using discontinuous Galerkin with the weighting function on element K_f denoted by $\boldsymbol{V}$. This leads to the DG weak form

$$\sum_{f=1}^{M} \left\{ \int_{K_f} (\boldsymbol{V} \cdot \mathbf{Q}_{,t} - \boldsymbol{V}_{,i} \cdot \mathbf{A}_i\mathbf{Q} - \boldsymbol{V} \cdot \mathbf{S}) \, d\mathbf{x} + \int_{\partial\Omega_f} \boldsymbol{V} \cdot \widehat{\mathbf{F}}'_n(\mathbf{y}^-, \mathbf{y}^+) \, d\mathbf{s} \right\} = 0 \quad (9)$$

where, again, all interface and boundary conditions are set through the numerical flux and we use a simple Lax–Friedrichs flux for $\widehat{\mathbf{F}'_n}(\mathbf{y}^-, \mathbf{y}^+)$. For the outer far-field boundary, $\mathbf{y}^+ = 0$ which is a first-order nonreflecting condition. On the coupling boundary Γ_c, $\mathbf{y}^+ = \mathbf{Y}(\mathbf{U}) - \overline{\mathbf{Y}}$ where $\mathbf{Y}(\mathbf{U})$ is the primitive solution vector corresponding to the conservative state vector $\mathbf{U}$ at the near-field edge.

Similar DG spatial discretizations are used for the adjoint equations (6) and (7) and the resulting weak forms can be found in [16]. As in the state equation coupling presented above, the adjoint Navier–Stokes and adjoint linearized Euler equations are coupled through the numerical fluxes along Γ_c.

Optimization

In order to solve the optimization problem, the multi-model state is first solved forward in time from t_0 to t_f and the state (in the near-field) is stored for use in the adjoint computation. The multi-model adjoint is then solved backward in time from t_f to t_0 and the resulting adjoint solution is used to evaluate the gradient of the objective function with-respect-to the control. This gradient is then used in a a nonlinear conjugate-gradient optimization algorithm with line-search globalization. Typically we solve the optimization problem to a fairly loose tolerance (such that the change in subsequent values of J is less than about 10^-3). Attempting to solve the problem to a tighter tolerance is typically nonproductive since the continuous adjoint based gradient is only accurate to the order of the truncation error in the discretization. Likewise, changes in J of less than 10^{-3} are typically not practically relevant.

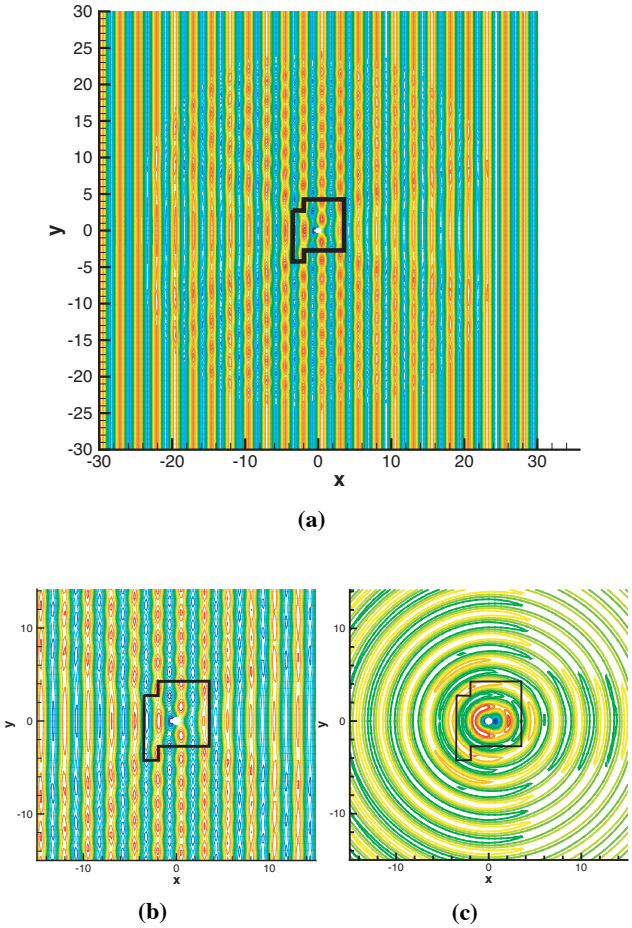

Fig. 3 Acoustic scattering from a circular cylinder: (a) Incident and scattered pressure on the full domain, (b) Incident and scattered pressure near the cylinder, (c) Scattered pressure near the cylinder. The irregular solid line denotes the interface between the Euler region in the near-field and the wave equation region in the far-field.

State Validation

As validation of our multi-model state solver, we consider the classical acoustics benchmark problem of planar acoustic wave scattering from a circular cylinder. We solve this problem using our multi-model approach with the Euler equation in the near-field coupled to the wave equation in the far-field and the numerical solutions are compared to the analytical result [21]. For this calculation, the reference length is the cylinder radius, the reference velocity is

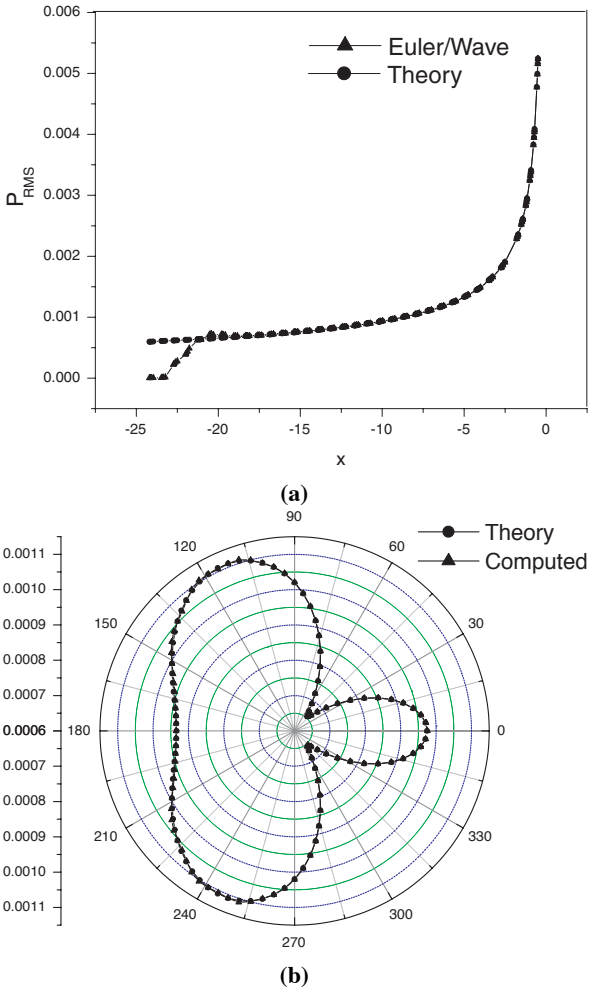

Fig. 4 Acoustic scattering from a circular cylinder: (a) Comparison of RMS pressure along the ray $\theta = \pi$, (b) Comparison of RMS pressure along radius $r = 10$ (that is outside the coupling interface).

the far-field acoustic speed, and all other reference values are based on far-field values. The incident plane-wave is expressed as $p_i = P_0 \exp[ik(x - ct)]$, where the direction of propagation is along the positive x-axis and $P_0 = 0.01$ is the incident pressure amplitude. Under these conditions, the scattered pressure wave is expressed by the following Bessel function expansion

$$P_s = \sum_{m=0}^{\infty} A_m \cos(m\theta)[J_m(kr) + iN_m(kr)]e^{-i\omega t},$$

where (r, θ) are the usual cylindrical coordinates, $\omega = 2\pi c/\lambda$,

$$A_m = -\varepsilon_m P_0 i^{m+1} e^{-i\gamma_m} \sin(\gamma_m),$$

and $\tan(\gamma_0) = -J_1(k)/N_1(k)$ as defined in [21].

The simulation is conducted for an incident acoustic wave with $k = 2.5$. The domain Ω is large $[-30, 30] \times [-30, 30]$ with a sponge layer enforced around the perimeter of the domain to approximate a nonreflecting boundary [22]. From Figure 3, it can be seen that an arbitrary interface (coincident with inter-element boundaries) is selected

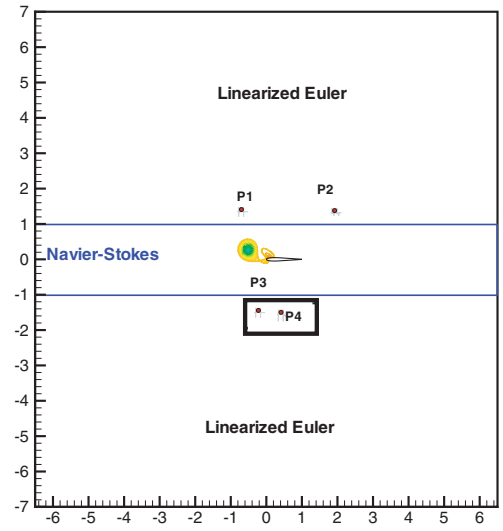

Fig. 5 Optimal control of BVI noise: problem setup

that separates the Euler domain in the near-field from the wave equation domain in the far-field.

Figure 3 shows contours of the instantaneous, pressure field from the simulation and smooth solutions are obtained near the coupling surface. In Figure 4, the RMS pressure from the scattered wave is compared with the analytical solution from inviscid theory and both the RMS pressure agrees with the theoretical results with no indication of inaccuracies near the coupling interface. This test case, demonstrates that our multi-model approach can accurately predict the intensity and directionality of acoustic wave scattered from a solid body. This and other validation cases [16, 23], give us confidence in our multi-model formulation.

BVI Model Problem

This section presents results for the optimal control of noise produced by the interaction of a vortex with a Bell AH1 rotor-blade in a uniform freestream. For this BVI problem, as shown in Figure 5, the computational domain is decomposed into three parts. In the middle region, the Navier–Stokes equations are used to model the nonlinear interaction between the vortex and rotor blade. In the upper and lower regions the linearized Euler equations are used to capture the scattered acoustics.

The initial condition is computed by superimposing a vortex on the steady-state solution of the Navier–Stokes equations for a uniform flow of freestream Mach number $M_\infty = 0.3$ over the Bell AH1 rotor-blade. The vortex is advected downstream by the freestream and interacts with the rotor blade in its path leading to a BVI type noise source.

A relatively strong Oseen vortex of circulation -0.5 and core radius $R_v = 0.15$ is superimposed on the uniform flow at location $(-6, 0.25)$ upstream of and above the rotor, where $(0, 0)$ corresponds to the leading edge of the rotor blade. The vortex is convected downstream by the flow while a relatively strong cylindrical acoustic wave travels

outward from the initial point of superposition. In order to allow the initial transient acoustic waves to leave the domain, we advance the solution for 1.36 time units and define this as our initial condition for optimization, $t_0 = 1.36$

Recall that the control objective (4) is to minimize the acoustic pressure intensity in the rectangular area depicted in Figure 5. Motivated by the success of Collis *et al.* [15] using boundary blowing/suction for the optimal control of aeroacoustic noise generated by vortex interacting with a circular cylinder, we use the time- and space-dependent distribution of surface normal velocity (suction/blowing) over the entire rotor surface as our control mechanism. Nakamura's work [24] indicates that the leading edge of the rotor blade plays a very important role in the interaction process. Likewise, through numerical simulation, Morvant [25] also shows that BVI is primarily a leading-edge phenomenon and the compressibility waves which propagate upstream above and below the rotor are generated from the large flow-deflections at the leading edge.

Based on these observations, we define our optimization time-window to capture only the leading-edge acoustics in order to reduce computational cost. Thus, the optimization time-window consists of $20,000$ uniform time-steps with $\Delta t = 8 \times 10^{-5}$ from time $t_0 = 1.36$ to $t_f = 2.96$. Four measurement stations are placed above and below the rotor blade to record the time-history of pressure fluctuations (see Figure 5).

Stations P_1 and P_2 are located in the linearized Euler subdomain above the blade to capture the upward traveling acoustics while stations P_3 and P_4 are located inside the observation region $\Omega_{\rm obs}$. Contours of scattered pressure at different time-instants are shown in Figure 6 both with and without control. With control, the intensity of acoustic pressure inside the observation region is reduced dramatically. Quantitatively, the value of J is reduced from 0.91 to 0.06 and the sound pressure level in the observation region is reduced by approximately 12dB.

However, the sound pressure level above the rotor blade upstream is strengthened as seen in Figure 6. This is more clearly observed in Figure 8, which plots the history of pressure fluctuations at stations P_1, P_2, P_3 and P_4. Compared with the uncontrolled pressure fluctuations at those four stations, the amplitude at P_3 and P_4, inside the observation region $\Omega_{\rm obs}$, is noticeably reduced. Near the end of the time-interval at P_4, there is a slight increase in the amplitude of the pressure fluctuations that is associated with acoustic waves generated as the vortex passes over the trailing edge of the rotor blade. Comparing the pressure fluctuations for uncontrolled and controlled flow in Figure 8, shows that there is a delayed effect of the control observed at all stations due to the finite sound speed.

Adjoint Analysis

To better understand the effect of wall-transpiration control, the evolution of adjoint variable λ_4 (in the near-field) and ξ_4 in the far-field, which contributes to the gradient information for the control update, is shown in Figure 7.

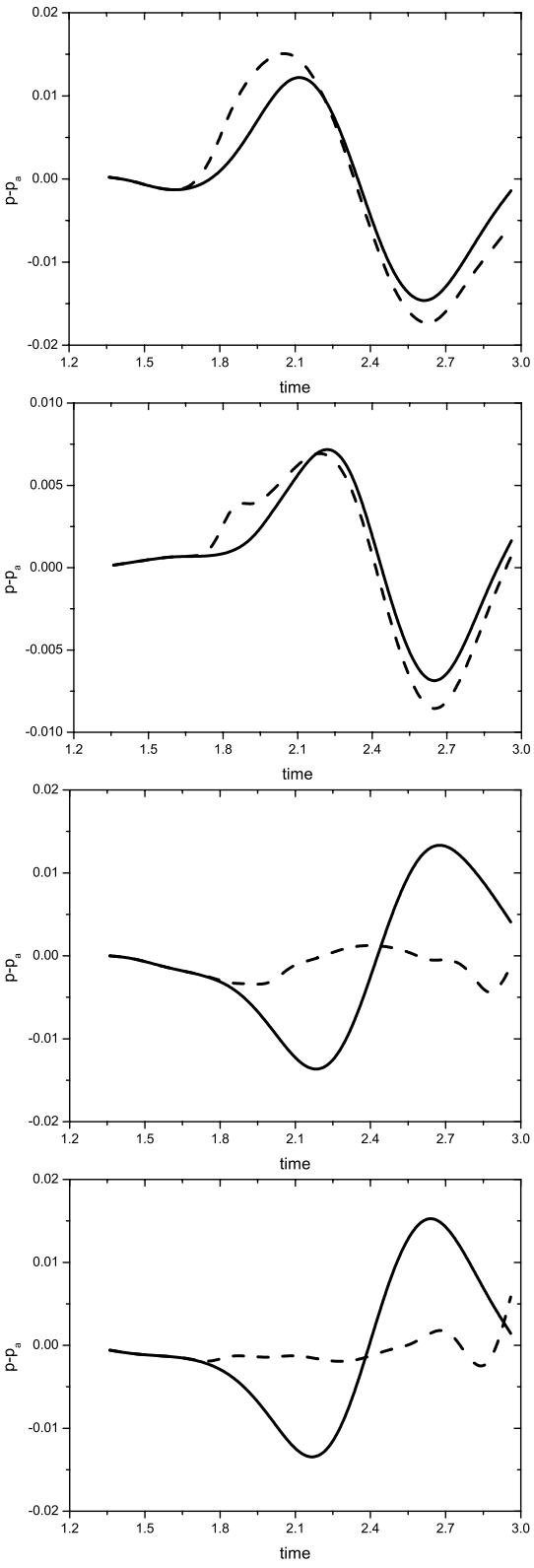

Fig. 8 Time history of pressure fluctuations at different stations. From top to bottom: station 1, station 2, station 3, station 4: ——— no control; - - - - optimal control.

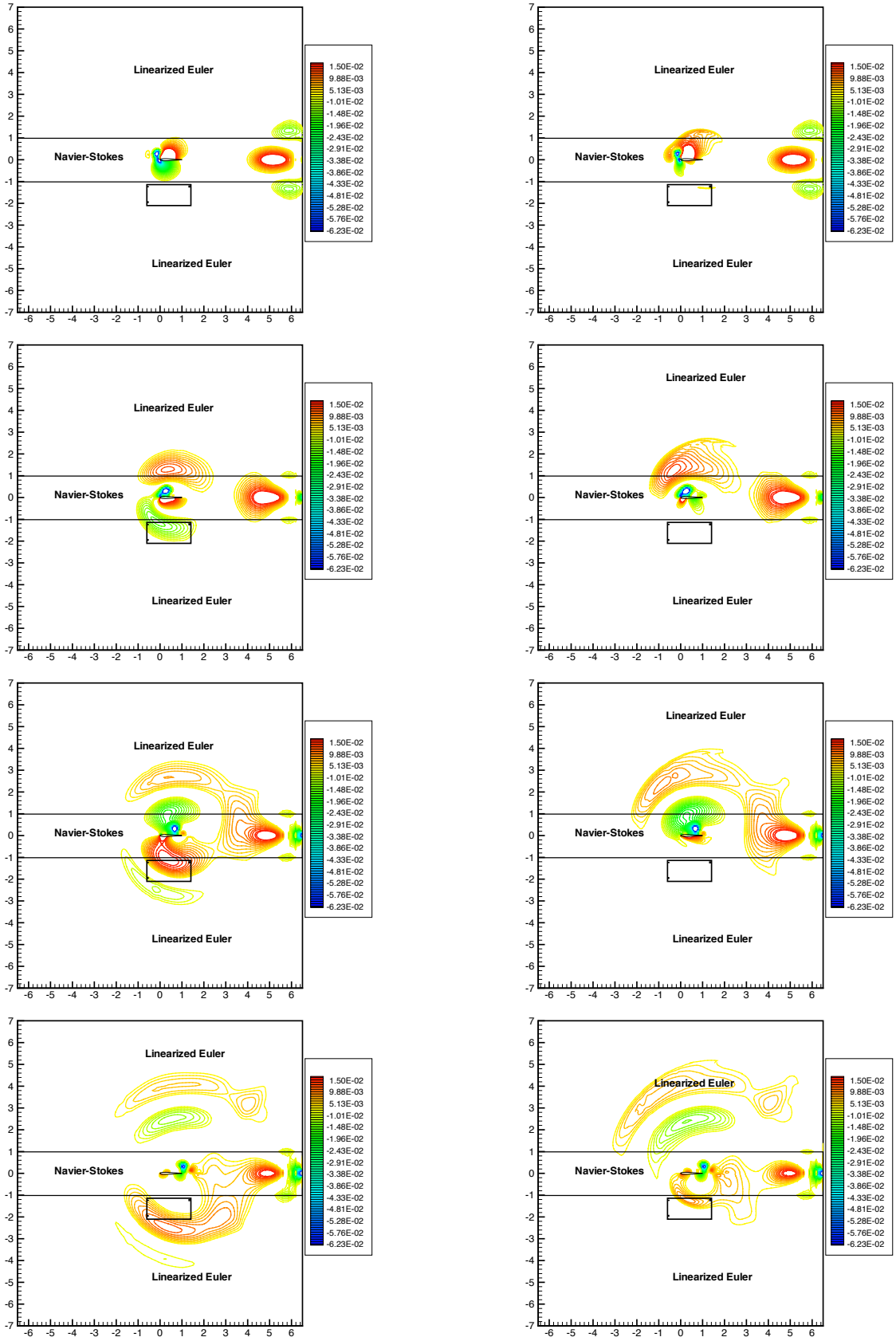

Fig. 6 Optimal control of BVI noise: contours of scattered pressure $p - p_a$ at instants $t = 1.78, 2.18, 2.58, 3.08$ for no-control (left) and control (right).

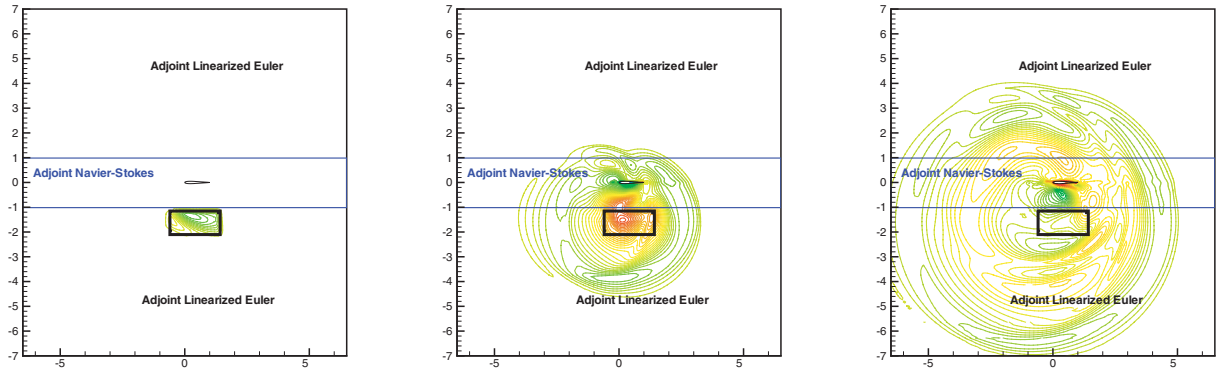

Fig. 7 Adjoint variable λ_4 in the near-field and ξ_4 in the far-field. Time goes backward in the adjoint solution (a) t=2.92, (b) t=2.16, (c) t=1.00.

This adjoint quantity is associated with an adjoint "acoustic wave" generated by pressure fluctuations in the observation region. As the adjoint wave moves outward from the observation region, it interacts with the rotor blade leading a non-zero adjoint field on the blade surface that corresponds to the gradient of the objective function with respect to the control. Given this qualitative behavior of the adjoint solution, such interaction between the control and the flow-field alters the far-field acoustics delicately by changing the near-field acoustic source. Figure 7 also shows that the adjoint solution around the coupling surface is quite smooth, indicating that our coupling approach for the adjoint equation is working properly.

Discussion

In order to understand the underlying mechanism of noise reduction, we consider the effect of the control on several important BVI parameters. Interestingly, two important parameters for BVI noise — vortex strength and miss distance — are not significantly changed. Without control, the vortex strength changes from -5.01 to -4.13 after passing the blade. With control, the vortex strength changes from -5.01 to -4.11 and the path is nearly identical as shown in Figure 9. Thus, the control appears to have a negligible effect on both the vortex trajectory and vortex strength.

Considering the direct relation between the strength of BVI noise levels and temporal pressure gradients near the leading-edge [26], we now explore the effect of control on the transient drag and lift histories. Figure 10 shows that the drag coefficient C_d is slight increased during the first half of the optimization interval, which appears to be associated with an increase in viscous stress due to the control on the rotor blade surface. During the second half of the optimization time-interval, there are only slight changes in the drag as the control is relatively weaker.

More relevant for BVI noise are the changes in lift coefficient C_l, which are primarily due to pressure differences on the blade surface. As observed by Peake and Crighton [27], the reduction of unsteady lift on the blade during a BVI event should, at least at low Mach number, lead to reduced sound generation. This observation has led to the

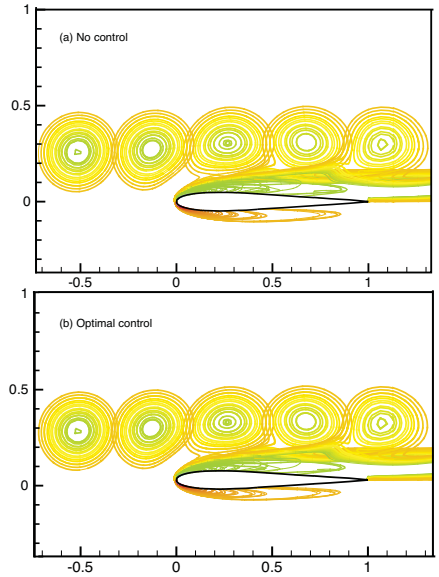

Fig. 9 Vortex trajectories with and without control.

use of oscillating trailing edge flaps [28–30] as well as suction/blowing on the blade surface [31, 32] to reduce the unsteady lift on rotor blades. Figure 11 shows that unsteady lift is noticeably reduced due to the control. More importantly, Figure 11 also shows that the temporal gradient of C_l is reduced which is directly related to the strength of BVI sound [26], and is consistent with the results shown in Figure 8.

Conclusions

We believe that this work is the first model-based effort using optimal control theory to construct controls that reduce BVI noise on a (relatively) realistic blade-vortex interaction (BVI) configuration. Our solutions are obtained using an efficient and novel multi-domain and multi-model method based on a high-order accurate discontinuous Galerkin discretization. This approach works well for both state and adjoint computations and leads to BVI control results that are quite promising. In particular, it is shown that optimal distributions of wall-normal suction and blowing can be obtained that significantly reduce

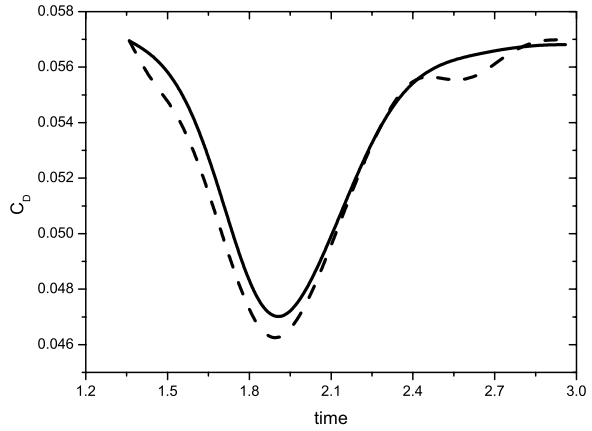

Fig. 10 Time history of drag coefficient C_d: ——— no control; – – – – optimal control.

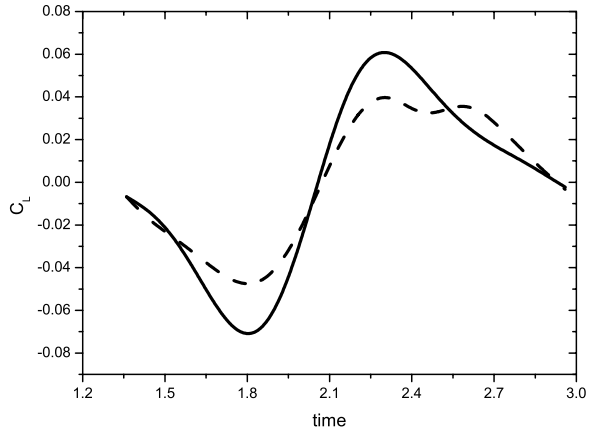

Fig. 11 Time history of lift coefficient C_l: ——— no control; – – – – optimal control.

downward radiated BVI noise. For the conditions studied here, a 12dB reduction in sound pressure level is obtained when the objective function targets downward radiated BVI sound. While the optimal control has negligible effect on both the vortex strength and trajectory, it does alter the interaction of the vortical and potential fields, which is the source of BVI noise. While this results in a slight increase in drag, there is a significant reduction in the temporal gradient of lift leading to a reduction in BVI sound levels.

Acknowledgments

This work is partially supported by Texas ATP grant 003604-0011-2001, NSF grant 0116289-2001, and the Department of Energy. The authors have benefited from helpful discussions with Dr. Kaveh Ghayour and Prof. Matthias Heinkenschloss, both of Rice University and Dr. Bart van Bloemen Waanders and Dr. Roscoe Bartlet of Sandia National Laboratories.

References

[1]Collis, S. S., Ghayour, K., and Heinkenschloss, M., "Optimal Control of Aeroacoustics: Transpiration Boundary Control," *AIAA J.*, Vol. 41, No. 7, July 2003.

[2]Chen, G. and Collis, S. S., "Toward Optimal Control of Aeroacoustic Flows using Discontinuous Galerkin Discretizations," *AIAA paper 2004-0364*, January 2004.

[3]Brentner, K. S. and Farassat, F., "An Analytical Comparison of the Acoustic Analogy and Kirchhoff Formulation for Moving Surfaces," *the American Helicopter Society 53rd Annual Forum*, 1997, Electronically available from http://techreports.larc.nasa.gov/ltrs/PDF/1998/jp/NASA-98-aj-ksb.pdf .

[4]A.S., L., "Review: The Use of Kirchhoff's Method in Computational Aeroacoustics," *Transactions of the ASME, Journal of Fluids Engineering*, Vol. 116, 1994, pp. 665–676.

[5]Farassat, F., "The Kirchhoff Formulas For Moving Surfaces in Aeroacoustics- The Subsonic and Supersonic Cases," Technical memorandum 110285, NASA, 1996, Electronically available from ftp://techreports.larc.nasa.gov/pub/techreports/larc/ 96/NASA-96-tm110285.ps.Z .

[6]Lighthill, M. J., "On Sound Generated Aerodynamically, I. General Theory,," *Proceedings of The Royal Society*, Vol. 221A, London, 1952, pp. 564–587.

[7]Williams, J. F. and Hawkings, D., "Sound Generation by Turbulence and Surfaces in Arbi-trary Motion," *Phil. Trans. Roy. Soc.*, 1969, pp. 321–342.

[8]Viswanathan, K. and Sankar, L. N., "Toward the Direct Calculation of Noise: Fluid/Acoustic Coupled Simulation," *AIAA Journal*, Vol. 33, No. 12, 1995, pp. 2271–2279.

[9]Djambazov, G., Lai, C., and Pericleous, K., "Development of a Domain Decomposition method for Computational Aeroacoustics," *DD9 Proceedings*, John Wiley & Sons, 1997, Electronically available from http://www.gre.ac.uk/ dg06/papers/norpap.ps.

[10]Djambazov, G., Lai, C., and Pericleous, K., "Efficient Computation of Aerodynamic Noise," *Comptemporary Mathematics*, Vol. 218, 1998, pp. 506–512, Electronically available from http://www.gre.ac.uk/ dg06/papers/colpap.ps.

[11]Djambazov, G., Lai, C., and Pericleous, K., "Staggered-Mesh Computation for Aerodynamic Sound," *AIAA Journal*, Vol. 38, 2000, pp. 16–21.

[12]Collis, S. S., Ghayour, K., Heinkenschloss, M., Ulbrich, M., and Ulbrich, S., "Towards Adjoint-Based Methods for Aeroacoustic Control," *AIAA Paper 2001-0821*, 2001.

[13]Collis, S. S., Ghayour, K., Heinkenschloss, M., Ulbrich, M., and Ulbrich, S., "Numerical Solution of Optimal Control Problems Governed by the Compressible Navier–Stokes Equations," *International Series of Numerical Mathematics*, Vol. 139, Birkhäuser Verlag, 2001, pp. 43–55.

[14]Collis, S. S., Ghayour, K., Heinkenschloss, M., Ulbrich, M., and Ulbrich, S., "Optimal Control of Unsteady Compressible Viscous Flows," *Inter. J. Num. Meth. Fluids*, Vol. 40, 2002, pp. 1401–1429.

[15]Collis, S. S., Ghayour, K., and Heinkenschloss, M., "Optimal Control of Aeroacoustic Noise Generated by Cylinder Vortex Interaction," *Int. J. Aero*, Vol. 1, No. 2, 2002, pp. 97–114.

[16]Chen, G., *Multimodel Simulation for Optimal Control of Aeroacoustics*, Ph.D. thesis, Rice University, Mechanical Engineering and Materials Science, 2004.

[17]Hager, W. W., "Runge–Kutta Methods in Optimal Control and Transformed Adjoint System," *Numerische Mathmatik*, Vol. 87, No. 2, 2000, pp. 247–282.

[18]Cockburn, B., Karniadakis, G., and Shu, C.-W., editors, *Discontinuous Galerkin Methods: Theory, Computation, and Applications*, Springer, 2000.

[19]Cockburn, B., editor, *High-order methods for computational applications, Lecture Notes in Computational Science and Engineering*, chap. Discontinuous Galerkin methods for convection-dominated problems, Springer, Berlin, 1999, pp. 69–224.

[20]Bassi, F. and Rebay, S., "A High-Order Accurate Discontinuous Finite Element Method for the Numerical Solution of the Compressible Navier–Stokes Equations," *J. Comp. Phys.*, Vol. 131, 1997, pp. 267–279.

[21]Morse, P. M. and Ingard, K. U., *Theoretical Acoustics*, Princeton University Press, 1968, pp. 400–405.

[22]Collis, S. S. and Lele, S. K., "A Computational Approach to Swept Leading-Edge Receptivity," *AIAA Paper 96-0180*, 1996.

[23]Chen, G. and Collis, S. S., "Heterogeneous Domain Decomposition for Aeroacoustic Computation," draft.

[24]Nakamura, Y., "Prediction of blade vortex interaction from measured blade pressure," *AHS Seventh European Rotorcraft Powered Lift*, 1981.

[25]Morvant, R., *The Investigation of Blade-Vortex Interaction Noise Using Computational Fluid Dynamics*, Ph.D. thesis, University of Glasgow, 2004.

[26]Boxwell, D. A., Schmitz, F. H., Splettstoeser, W. R., and Schultz, K. J., "Model Helicopter Rotor High-Speed Impulsive Noise: Measured Acoustics and Blade Pressures," *the Ninth European Rotorcraft Forum*, Stresa, Italy, 1983.

[27]Peake, N. and Crighton, D. G., "Active Control of Sound," *Annual Review of Fluid Mechanics*, Vol. 32, 2000, pp. 137–164.

[28]Kerschen, E. J., "Active aerodynamic control of wake-airfoil interaction noise theory," *DGLR/AIAA Paper 92-02-039*, 1992.

[29]Simonich, J. C., Lavrich, P., Sofrin, T. G., and Topol, D. A., "Active aerodynamic control of wake-airfoil interaction noise-experiment," *DGLR/AIAA Paper 92-02-038*, 1992.

[30]Parameswaran, V. and Baeder, J., "Reduction of Blade Vortex Intera ction Noise Using Prescribed Pitching," *AIAA Paper 96*, 1995.

[31]Lee, S., "Reduction of Blade-Vortex Interaction Noise Through Porous Leading Edge," *AIAA Journal*, Vol. 32, No. 3, 1994, pp. 480–488.

[32]Straub, A. A. H. F. K. and Charles, B. D., "Effects of Surface Blowing/Suction on the Aerodynamics of Helicopter Rotor Blade-Vortex Interactions (BVI) – A Numerical Simulation," *The Journal of the American Helicopter Society*, 1997.